ACS APPLIED MATERIALS & INTERFACES

www.acsami.org

Research Article

Buried Interface Passivation with 3,4,5-Trifluorophenylboronic Acid Enables Efficient and Stable Inverted Perovskite Solar Cells

Jiansheng Yang, Zhenhua Zhao, Changzeng Ding,* Lianping Zhang, Xiaomei Gao, Rong Huang, Zhiyun Li, Qun Luo, Bin Fan, Qingyong Tian, Lingpeng Yan, Kunpeng Guo, Yongzhen Yang,* and Chang-Qi Ma*

Cite This: *ACS Appl. Mater. Interfaces* 2025, 17, 16844−16854

Read Online

ACCESS | Metrics & More | Article Recommendations | Supporting Information

ABSTRACT: The p-i-n type perovskite solar cells with a nickel oxide (NiOx) hole transport layer in combination with self-assembled monolayers (SAMs) have a high power conversion efficiency (PCE) of over 26%. The surface properties of the SAM layer have a significant impact on the growth and crystallization of the perovskite film. In the meanwhile, defects formed during thermal annealing at the SAM layer and the perovskite layer interface would act as charge recombination centers, decreasing device performance and stability. To address these issues, this work introduces 3,4,5-trifluorophenylboronic acid (3,4,5-3FPBA) as the interfacial modification layer to improve the buried interface properties that enable better crystallization of the perovskite film. With the 3,4,5-3FPBA layer, based on the perovskite composition $Cs_{0.05}(FA_{0.98}MA_{0.02})_{0.95}Pb(I_{0.95}Br_{0.05})_3$, the device efficiency increased from 21.99% to 24.02%. A similar improvement was observed for the perovskite composition $Cs_{0.05}FA_{0.82}MA_{0.13}Pb(I_{0.85}Br_{0.15})_3$, where the device efficiency increased from 21.87% to 22.76%. The universality of interface modification has been confirmed. In addition, based on the perovskite composition $Cs_{0.05}FA_{0.82}MA_{0.13}Pb(I_{0.85}Br_{0.15})_3$, the resulting cells showed improved thermal stability, maintaining 75% of its initial efficiency after 500 h of continuous heating at 85 °C for unencapsulated devices.

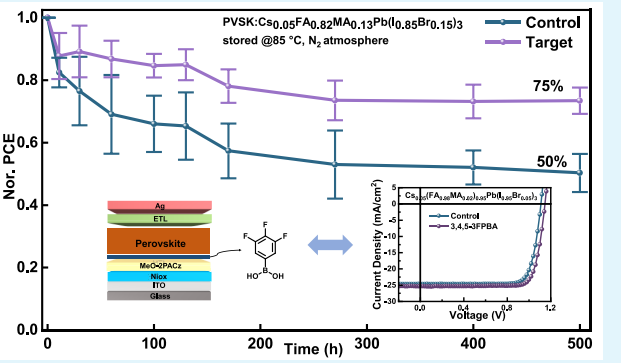

KEYWORDS: *perovskite solar cells, 3,4,5-trifluorophenylboronic acid, self-assembled monolayer, thermal stability, power conversion efficiency*

1. INTRODUCTION

As a rising star in the photovoltaic technology, perovskite solar cells (PSCs) has attracted widespread attention for their high power conversion efficiency (PCE),[1,2] low manufacturing cost,[3,4] and flexible large-area preparation.[5,6] Currently, the PCE of inverted (p-i-n) PSCs has exceeded 26%,[7] demonstrating tremendous development potential and commercial application values. In reviewing the development of inverted-type PSCs, the hole transport material (HTM) is the key factor in achieving high PCE.[8−10] The HTM for inverted PSCs have shifted from traditional materials, including poly[bis(4-phenyl)(2,4,6-trimethylphenyl)amine] (PTAA),[11,12] poly(3,4-ethylenedioxythiophene):poly(styrenesulfonate) (PEDOT:PSS),[13,14] and NiOx,[15−17] to distinctive self-assembling material (SAM), such as 2-(9*H*-carbazol-9-yl)ethyl phosphonic acid (2PACz),[18−20] [2-(3,6-dimethoxy-9*H*-carbazol-9-yl)-ethyl]phosphonic acid (MeO-2PACz),[21,22] and [4-(3,6-dimethyl-9*H*-carbazol-9-yl)butyl]phosphonic acid (Me-4PACz).[23,24] These materials show the advantages of high hole-selectivity,[17,25] high hole transport efficiency,[19,26] and low interface defects,[3,27] resulting in high efficiency of p-i-n type PSCs.

It has been found that devices using NiOx as hole transport layer (HTL) exhibit high stability but low efficiency.[15,17] Conversely, devices with SAM as HTL possess high efficiency but lack stability.[18−20] Therefore, researchers have combined the two type materials as dual HTL to achieve devices with both high efficiency and stability.[28] However, the dual HTL can only address the issue of SAM weak anchoring to the substrate but cannot solve the interfacial problems between SAM and perovskite.[29] The specific interfacial issues mainly include: (1) different SAM materials have various dipole moments, leading to different interface contacts; (2) the film-

Received: December 9, 2024
Revised: February 24, 2025
Accepted: February 28, 2025
Published: March 7, 2025

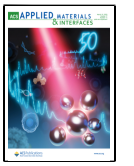

https://doi.org/10.1021/acsami.4c21627
ACS Appl. Mater. Interfaces 2025, 17, 16844−16854

forming process of SAM materials results in a rough surface that is harmful to the growth and crystallization of perovskite. These factors can lead to a decrease in the device performance. To address these issues, researchers have optimized the molecular structure of the SAM with suitable dipole moments. When applied to devices, these materials have a suitable energy level matching perovskite, enhancing charge collection and suppressing interfacial reactions and recombination, ultimately achieving high efficiency and stability.[22,27,29−32] Other researchers focused on the interface, inserting a modification layer to improve film quality of perovskite substrates and boost device efficiency and stability.[20,33]

Based on this, 3,4,5-trifluorophenylboronic acid (hereinafter referred to as 3,4,5-3FPBA) was conducted as an interfacial modification layer between the SAM layer and the perovskite layer. It can passivate interfacial defects and provide a suitable growth substrate for the growth and crystallization of perovskite. Ultimately, the device modified with 3,4,5-3FPBA reached 22.76% [open-circuit voltage (V_{OC}) of 1.185 V], while the efficiency of the reference device was only 21.87% (V_{OC} of 1.164 V) based on the $Cs_{0.05}FA_{0.82}MA_{0.13}Pb(I_{0.85}Br_{0.15})_3$ perovskite system. After continuous heating at 85 °C for 500 h, the efficiency of the reference device dropped to 50% of its initial efficiency, while the efficiency of the 3,4,5-3FPBA-modified device remained at 75% of its initial efficiency.

2. EXPERIMENTAL SECTION

2.1. Materials. Lead(II) iodide (PbI_2) and lead(II) bromide ($PbBr_2$), CsI, formamidinium iodide (FAI), methylammonium bromide (MABr), phenethylammonium chloride (PEACl), and bathocuproine (BCP) were purchased from Xi'an Polymer Light Technology in China. NiOx nanoparticle powder and (6,6)-phenyl C61 butyric acid methyl ester ($PC_{61}BM$) were purchased from Advanced Election Technology Company in China. [2-(3,6-Dimethoxy-9*H*-carbazol-9-yl) ethyl] phosphonic acid (MeO-2PACz), 3,4,5-trifluorophenylboronic acid (3,4,5-3FPBA), 3,5-difluorophenylboronic acid (3,5-2FPBA), and 2,3,4,5,6-pentafluorobenzeneboronic acid (2,3,4,5,6-5FPBA) were purchased from TCI AMERICA in China. Dimethylformamide (DMF, purity >99%), dimethyl sulfoxide (DMSO, purity >99%), ethanol, isopropyl alcohol (IPA, purity >99%), and chlorobenzene (CB, purity >99%) were purchased from J&K scientific. All materials were used directly.

2.2. Preparation of Device. ITO glass substrate was cleaned by sequentially washing with detergent, deionized water (twice), and ethanol (twice). Before use, the ITO was treated with ultraviolet ozone for 30 min. Then, a thin layer of NiOx nanoparticle film (20 mg/mL NiOx water solution) was deposited on the ITO substrate by spin coating at 4000 rpm for 30 s and annealed in ambient air at 150 °C for 20 min. 0.5 mg/mL MeO-2PACz was deposited on the NiOx at 4000 rpm for 30 s and annealed at 100 °C for 10 min. 0.5 mg/mL 3,4,5-3FPBA was coated on the MeO-2PACz surface at 5000 rpm for 20 s. For $Cs_{0.05}FA_{0.82}MA_{0.13}Pb(I_{0.85}Br_{0.15})_3$ perovskite films, 1.5 M perovskite precursor solution was prepared through dissolving 190.12 mg of FAI, 548.6 mg of PbI_2, 77.07 mg of $PbBr_2$, 21.84 mg of MABr, and 17.68 mg of CsI in mixed solvents of DMF and DMSO (v/v: 4:1). The perovskite precursor solution was spin-coated on the substrate at 5000 rpm for 30 s; 230 μL of EA was dropped into the perovskite film at 10 s before ending the program; then the perovskite films were annealed at 120 °C for 30 min. For $Cs_{0.05}(FA_{0.98}MA_{0.02})_{0.95}Pb(I_{0.95}Br_{0.05})_3$ perovskite films, 1.7 M perovskite precursor solution was prepared through dissolving 277 mg of FAI, 781.4 mg of PbI_2, 12.9 mg of $PbBr_2$, 3.8 mg of MABr, and 22.5 mg of CsI in mixed solvents of DMF and DMSO (v/v: 6:1). The perovskite precursor solution was spin-coated on the substrate at 5000 rpm for 30 s, 170 μL of CB was dropped into the perovskite film at 15 s before ending the program, and then the perovskite films were annealed at 120 °C for 20 min. After that, 1 mg/mL PEACl was coated on the perovskite surface at 5000 rpm for 20 s and annealed at 100 °C for 10 min, then 20 mg/mL $PC_{61}BM$ was spin-coated at 3000 rpm 30 s, afterward, the BCP solution in IPA (0.5 mg/mL) was spin-coated on $PC_{61}BM$ film at 5000 rpm for 30 s. Finally, a 100 nm Ag electrode was thermally evaporated on the BCP film under vacuum of 6×10^{-4} Pa. The preparation of TCO thin films was carried out using magnetron sputtering, with the primary components of the film being In (indium) and W (tungsten) in a ratio of 98:2. The complete device was placed into a vacuum chamber, and the film was formed under the bombardment of high-energy particles. After 30 min of sputtering, the final film thickness reached 150 nm. Specifically, the thicknesses of each transport layer film were determined through relevant scanning electron microscopy (SEM) and atomic force microscopy (AFM) techniques, and the results are listed in Figure S1 and Table S1.

2.3. DFT Calculations. DFT calculations were performed with the ORCA 5.0.3 software package. The geometry optimizations were performed using the B3YP functional with the Becke-Johnson damping scheme (D3BJ), and the def2-SV(P) basis was used for all atoms. All calculations utilized the def2/J auxiliary basis. Electrostatic potential grid data files are generated with the Multiwfn program and visualized with the VMD program.

2.4. Instruments and Characterization. The current density−voltage (J−V) characteristics of the solar cell were measured with Keithley 2400 source in an N_2 glovebox in a simulated solar AM1.5G (Newport VeraSol-2 LED Class AAA solar simulator). The active area of each cell is 0.09 cm^2, and a 0.0625 cm^2 mask is used for J−V testing. The hysteresis coefficient at different scan rates is obtained by adjusting the Trigger Delay and Volt Speed NPLC values. At the same time, the scanning range is observed from 1.3 to −0.2 V and from −0.2 to 1.3 V. The electrochemical impedance spectroscopy was obtained by testing with an electrochemical workstation (PGSTAT302N) under dark open-circuit voltage. The frequency range is 0.1 Hz to 10 MHz. The external quantum efficiency (EQE) was measured by using a self-assembled system. This system consists of a 150 W tungsten lamp (Osram 64642), a monochromator (Zolix Omni l300), an optical chopper, and an I−V converter (QE-IV Convertor, Suzhou Deruikeyi Instrument Equipment Co., Ltd.) equipped with a lock in amplifier (Stanford Research Systems SR 830). To better simulate sunlight, the bias light of a 532 nm solid state laser was introduced into the testing system. During the test, a standard silicon cell was used as the reference cell for calibration. SEM images were obtained by a field emission scanning electron microscope (S-4800) at an accelerating voltage of 10 kV. The XRD spectra of the perovskite films were obtained by a Bruker D8 ADVANCE X-ray diffractometer with Cu Kα radiation (λ = 0.15418 nm). Absorption curves of samples were measured by an UV−vis spectrometer (LAMBDA 750, PerkinElmer). PL and TRPL of cells were measured by a homemade defect imaging system (LBIC). The thermal stability of unencapsulated devices was tested in a glovebox (H_2O < 10 ppm, O_2 < 10 ppm) with a thin-film solar cell decay test system (PVLT-G8001 M, Suzhou D & R Instruments) under 85 °C heating conditions. Absorbance and transmittance spectra were recorded with an UV/vis/near-IR spectrophotometer (PerkinElmer, LAMBDA 750). The AFM images were taken with a Dimension Icon. The SIMS data were tested through IONTOF TOF SIMS 5−100 (GmbH) with a GCIB sputter source with a 30 keV energy at Vacuum Interconnected Nanotech Workstation (Nano-X) of SINANO. The operational stability of the cells was tested on a multichannel solar cell performance degradation test system (PVLT-G8001 M, D&R Instruments Suzhou) in an N_2-filled glovebox (H_2O < 10 ppm, O_2 < 10 ppm) under a simulated white LED light (D&R Light, L-W5300KA-150, D&R Instruments Suzhou). The battery was irradiated with a white LED light (D&R Light, L-W5300KA-150, Suzhou D&R Instruments) at the intensity of a simulated sun (initial short current equal to the J_{SC} measured under standard conditions). The performance of the cell was measured by an I−V scan from 1.3 to −0.2 V in steps of 0.01 V. The temperature is measured from time to time and is approximately 55 to 65 °C. Unless otherwise specified, the subsequent device fabrication, characterization methods, and stability

https://doi.org/10.1021/acsami.4c21627
ACS Appl. Mater. Interfaces 2025, 17, 16844−16854

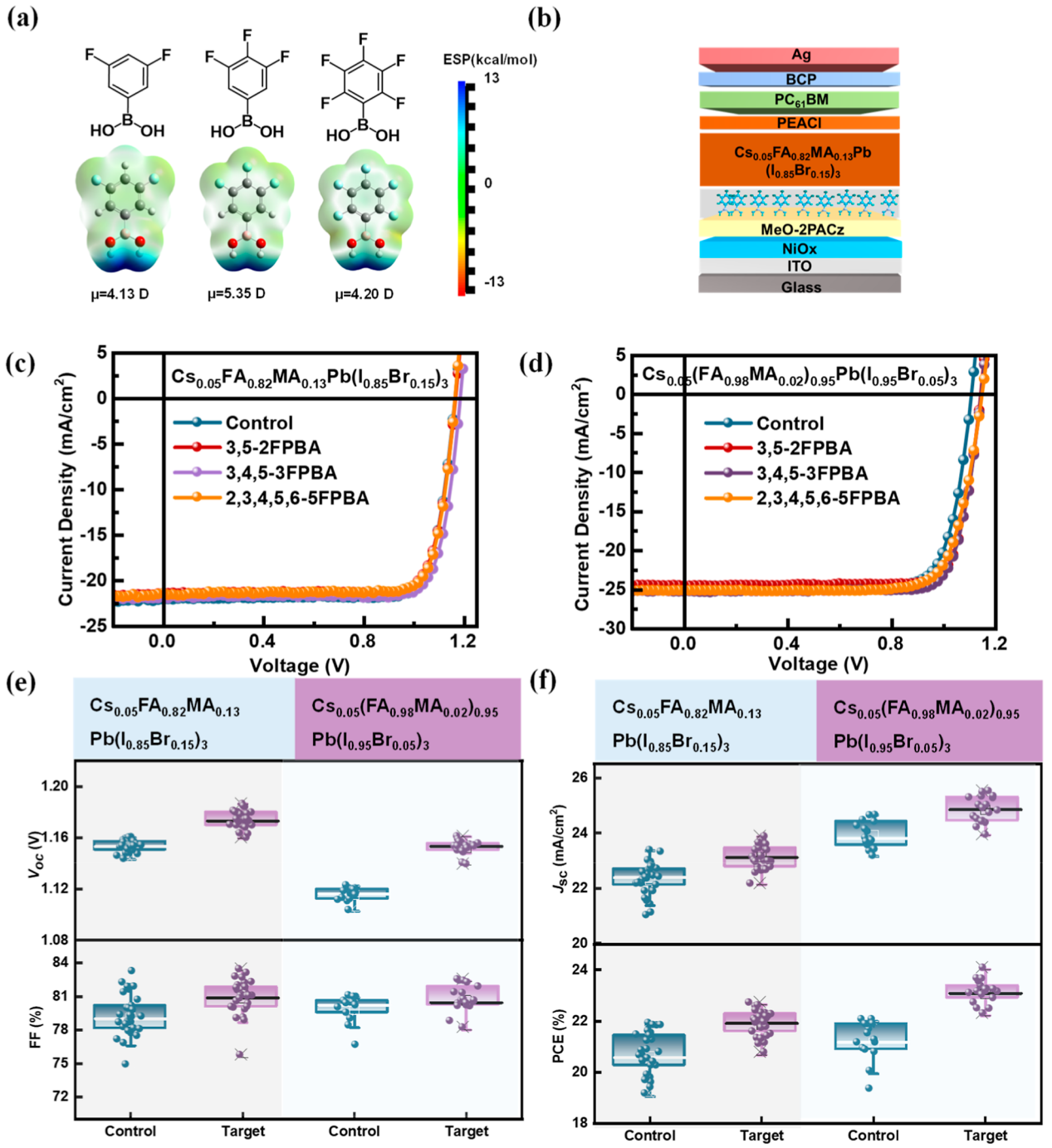

Figure 1. (a) Chemical structure and DFT calculated dipole forces of 3,5-2FPBA, 3,4,5-3FPBA, and 2,3,4,5,6-5FPBA; (b) schematic diagram of the p-i-n device structure; (c) optimal $J-V$ curves of devices modified with 3,5-2FPBA, 3,4,5-3FPBA, and 2,3,4,5,6-5FPBA based on the perovskite composition $Cs_{0.05}FA_{0.82}MA_{0.13}Pb(I_{0.85}Br_{0.15})_3$; (d) optimal $J-V$ curves of devices modified with 3,5-2FPBA, 3,4,5-3FPBA, and 2,3,4,5,6-5FPBA based on the perovskite composition $Cs_{0.05}(FA_{0.98}MA_{0.02})_{0.95}Pb(I_{0.95}Br_{0.05})_3$; performance distribution of (e) V_{OC} and FF and (f) J_{SC} and PCE of the control and target devices (3,4,5-3FPBA medicated), the data were averaged based on 32 individual devices.

tests are all based on the $Cs_{0.05}FA_{0.82}MA_{0.13}Pb(I_{0.85}Br_{0.15})_3$ perovskite system.

3. RESULTS AND DISCUSSION

3.1. Effect of Phenylboronic Acid Materials on the Device Performance. It was reported that fluorobenzene boronic acid can passivate the defects of the perovskite film by forming ionic bonds of F with Pb^{2+} and FA^+ ions in perovskite.[34,35] Therefore,3,5-difluorophenylboronic acid (3,5-2FPBA), 3,4,5-3FPBA, and 2,3,4,5,6-pentafluorobenzeneboronic acid (2,3,4,5,6-5FPBA) (Figure 1a) were used as interface modification layer for device fabrication. The schematic diagram of the device structure is shown in (Figure 1b). Based on the perovskite composition $Cs_{0.05}FA_{0.82}MA_{0.13}Pb(I_{0.85}Br_{0.15})_3$, the $J-V$ curves (Figure 1c) results demonstrate an enhancement in device performance following 3,4,5-3FPBA treatment. According to Table 1 and Figure S2 (1), the control, 3,5-2FPBA, 3,4,5-3FPBA, and 2,3,4,5,6-5FPBA modified cells exhibited optimum efficiencies of 21.87%, 22.18%, 22.76%, and 22.28%, respectively. Clearly,

https://doi.org/10.1021/acsami.4c21627
ACS Appl. Mater. Interfaces 2025, 17, 16844−16854

Table 1. Best and Average Photovoltaic Performance of the Control and FPBA-Modified Cells[a]

sample	V_{OC} (V)	J_{SC} (mA/cm^2)[b]	FF (%)	PCE (%)
control	1.164	23.05	81.50	21.87
	1.153 ± 0.007	22.57 ± 0.46	79.89 ± 3.03	20.79 ± 0.73
3,5-2FPBA	1.166	23.27	81.76	22.18
	1.158 ± 0.007	22.84 ± 0.45	79.00 ± 4.51	20.89 ± 1.27
3,4,5-3FPBA	1.185	23.47	81.84	22.76
	1.171 ± 0.009	22.90 ± 0.35	80.12 ± 3.24	21.48 ± 0.73
2,3,4,5,6-5FPBA	1.162	23.39	81.99	22.28
	1.158 ± 0.014	22.99 ± 0.40	79.92 ± 2.40	21.28 ± 1.11

[a]The average data were obtained from 32 individual cells. [b]J_{SC} data obtained from $J-V$ measurements, where light intensity was calibrated with certified Si solar cells.

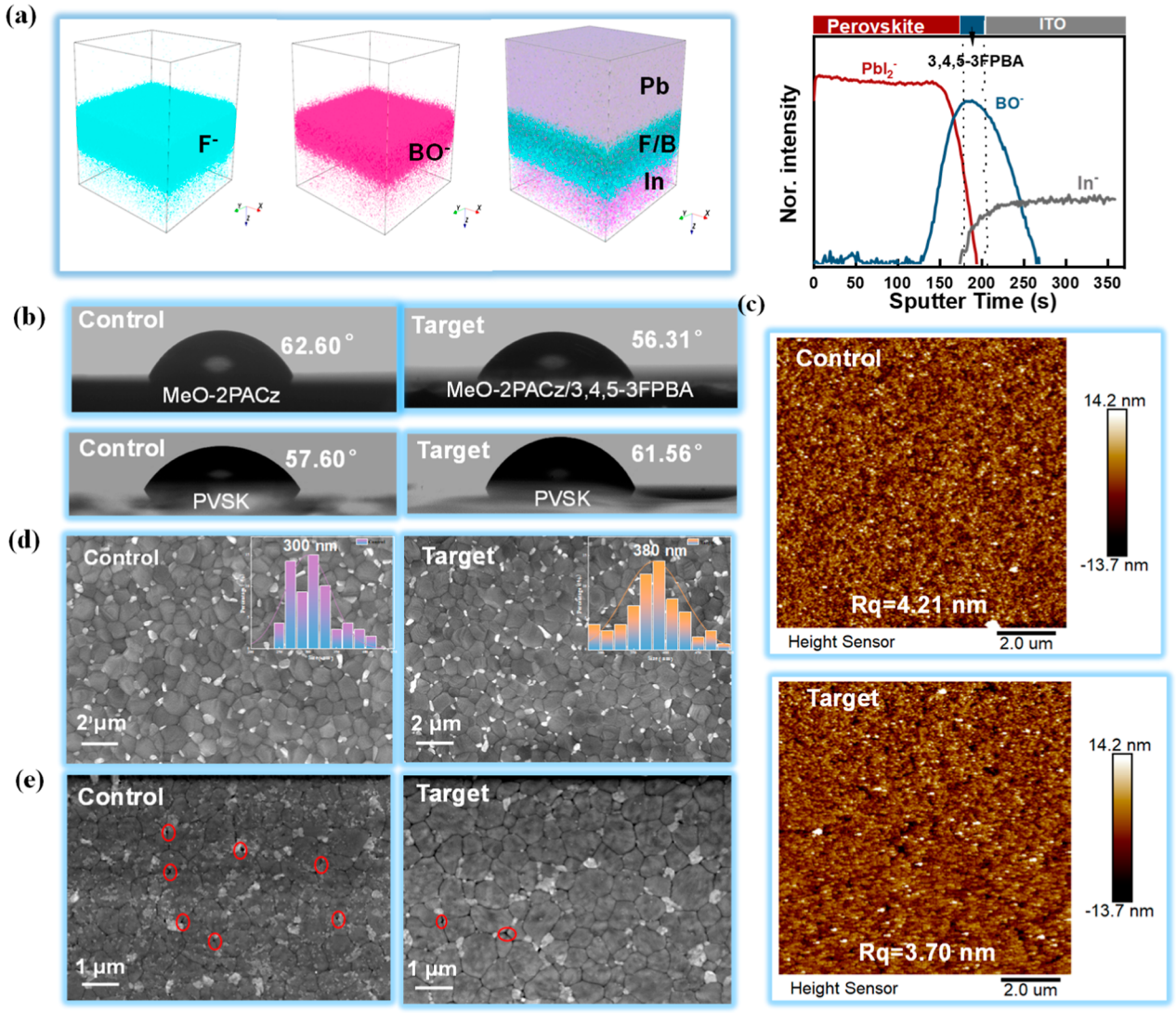

Figure 2. (a) TOF-SIMS testing revealed the distribution of PbI-2, BO^-, and In^- ions, along with corresponding 3D ion distribution maps; (b) water contact angles for the control and target films; (c) AFM images of films; (d) SEM images of the top interface of PVSK films, with insets showing the grain size distribution based on 100 samples; and (e) SEM images of the buried interface of PVSK films.

the device modified with 3,4,5-3FPBA shows the best efficiency; (2) the V_{OC} of control, 3,5-2FPBA, 3,4,5-3FPBA, and 2,3,4,5,6-5FPBA is 1.164, 1.166, 1.185, and 1.162 V. It is indicated that 3,4,5-3FPBA enhances device efficiency by improving the V_{OC}, possibly due to molecular dipole interactions. To assess the universality of the interfacial modification layer, devices were fabricated using another perovskite composition. The highest efficiency was achieved with the perovskite system based on $Cs_{0.05}(FA_{0.98}MA_{0.02})_{0.95}Pb(I_{0.95}Br_{0.05})_3$. According to Figure 1d and Table S2, the V_{OC} and PCE also show similar results after interfacial modification, indicating that the FPBA interfacial modification is universal. In addition, a 500 min short-term thermal stability test was carried out on four groups

https://doi.org/10.1021/acsami.4c21627
ACS Appl. Mater. Interfaces 2025, 17, 16844−16854

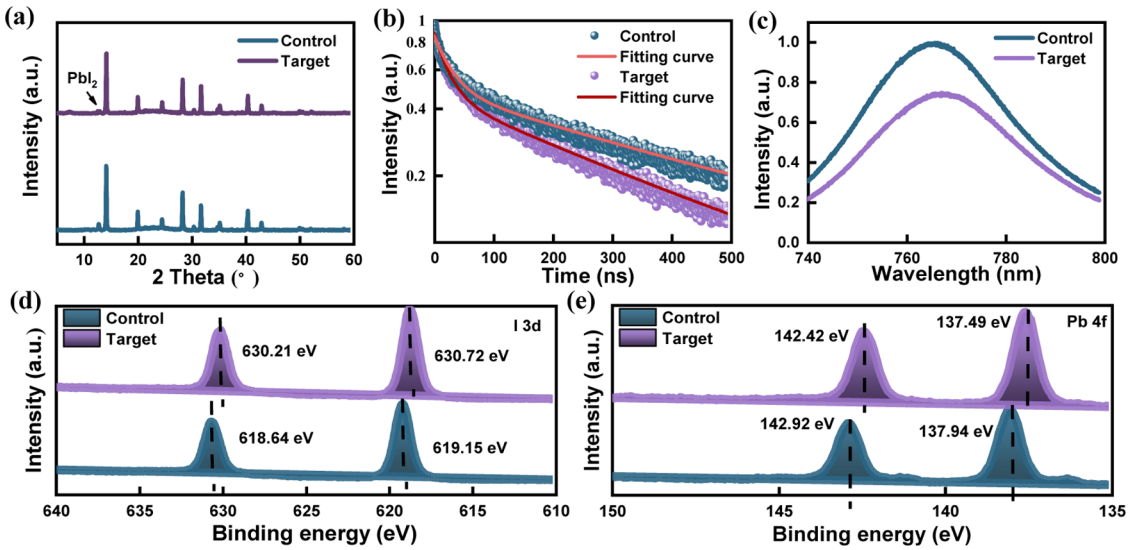

Figure 3. (a) XRD images of control and target PVSK films; (b) transient PL spectra and (c) steady-state PL spectra of perovskite films deposited on glass/NiOx/MeO-2PACz with or without 3,4,5-3FPBA interlayer, the film was excited from the glass side with a λ of 532 nm; and XPS spectra of I 3d (d) and Pb 4f (e) for the two perovskite films.

of devices, and a normalized data plot was drawn based on the test data. As shown in Figure S3, the device in the control group maintains 50% of its initial efficiency after heating. However, after continuous heating, the devices with 3,5-2FPBA, 3,4,5-3FPBA, and 2,3,4,5,6-5FPBA interface modifications maintain 60%, 90%, and 47% of their initial efficiencies, respectively. It can be seen that only the device modified with 3,4,5-3FPBA exhibits excellent stability, while the devices modified with 3,5-2FPBA and 2,3,4,5,6-5FPBA show poor stability. This may be related to the number and position of the fluorine atom sites. An inappropriate interface modification layer can cause an unstable interface and result in a decrease in the device stability.

Further statistical analysis (Figure 1e,f) of the data reveals significant enhancement of various device performances after 3,4,5-3FPBA modification. Additionally, forward (−0.2 to 1.3 V) and reverse (1.3 to −0.2 V) scan tests were conducted on the aforementioned devices to characterize their hysteresis performance; the scan rate for both the forward and reverse scans is 0.01 V/s. The results (Figure S4) show that the device of control, 3,5-2FPBA, 3,4,5-3FPBA, and 2,3,4,5,6-5FPBA hysteresis index of 8.7, 8.8, 7.2, and 10.01. This indicates that 3,4,5-3FPBA can reduce the hysteresis index of the device. At the same time, to ensure the universality of the interface modification layer in reducing device hysteresis, forward and reverse $J-V$ tests at different scan rates were conducted on both the control and target devices (Figure S5 and Table S3). The results show that after modification with 3,4,5-3FPBA, the hysteresis coefficients of the devices are lower than those of the unmodified devices and the hysteresis coefficients are smaller under both low-speed and high-speed scan tests.

To investigate the effectiveness of interface modification during the device scaling process, a 1 cm^2 device was fabricated using 3,4,5-3FPBA as a representative material. As shown in Figure S6 and Table S4, after the interface modification with 3,4,5-3FPBA, the efficiency of the device significantly increased. Further performance analysis of the device parameters reveals that both the open-circuit voltage (average V_{OC} increased from 1.056 to 1.077 V) and the fill factor (average FF increased from 69.10% to 75.11%) changed notably. Comparing with the small-area device performance, the interface modification remains effective during the scaling process and suppresses the decrease in FF. This is beneficial for the large-area commercial application of PSCs.

To preliminarily understand the reasons for the increase in V_{OC} and the decrease in the hysteresis of devices, density function theory (DFT) theoretical simulations (Figure 1a) were conducted on three fluorinated phenylboronic acid materials. The results revealed that the dipole moments of 3,5-2FPBA, 3,4,5-3FPBA, and 2,3,4,5,6-5FPBA are 4.13, 5.35, and 4.20 D, respectively. The 3,4,5-3FPBA intermediate layer exhibits a strong dipole moment and form a homogeneous junction structure that is conducive to the extraction of holes, which is consistent with literature reports.[36] The relatively high dipole moment of 3,4,5-3FPBA is then ascribed to the high V_{OC} of the cells, demonstrating that 3,4,5-3FPBA is a suitable interfacial material for PSCs.

3.2. Impact of 3,4,5-3FPBA on the Crystallization of Perovskite Films. To confirm the persistence of the 3,4,5-3FPBA interfacial modification layer during the formation of the perovskite film, samples with the structure of ITO/3,4,5-3FPBA/PVSK were prepared and subjected to the time of flight secondary ion mass spectrometry (TOF-SIMS) test (Figure 2a). The measured BO^- signal confirms the presence of the 3,4,5-3FPBA interface layer. Ultraviolet−visible spectra (UV−vis) and transmittance spectra (Figures S7 and S8) are almost identical for these two films, indicating that the introduction of 3,4,5-3FPBA does not influence the perovskite thin-film quality.

To further analyze the impact of 3,4,5-3FPBA as an interfacial modification layer on the microscopic morphology of SAM, water contact angle and AFM tests were conducted. Figure 2b shows that after introducing the 3,4,5-3FPBA interface modification layer, the water contact angle of the SAM surface decreased from 62.60 to 56.31°, while the water contact angle of the perovskite surface increased from 57.60 to 61.56°. On the one hand, the reduced water contact angle on the SAM surface provides a favorable substrate for perovskite growth and crystallization. On the other hand, the increased water contact angle on the perovskite surface indicates that the

https://doi.org/10.1021/acsami.4c21627
ACS Appl. Mater. Interfaces 2025, 17, 16844−16854

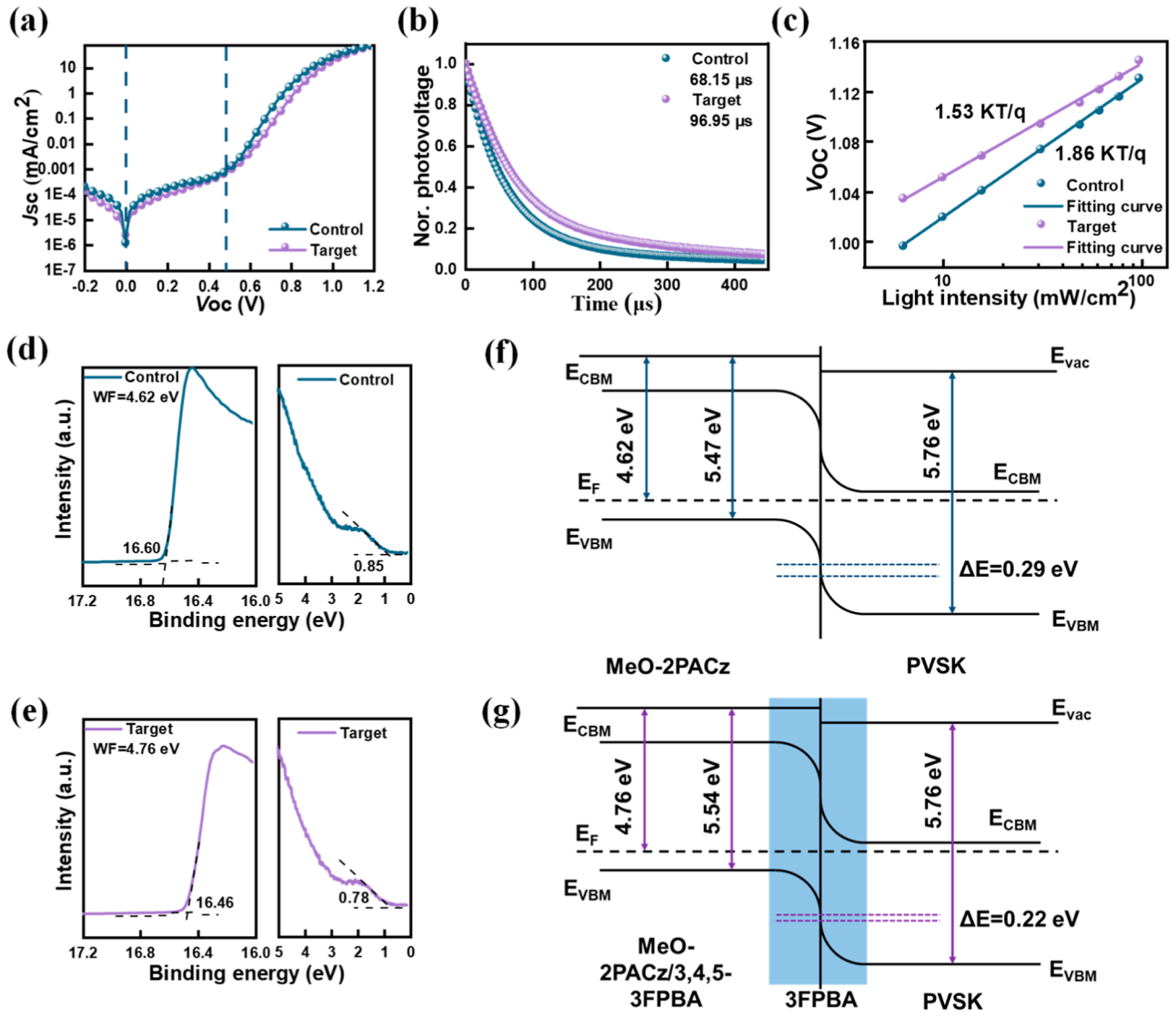

Figure 4. (a) Dark $J-V$ curve, (b) transient photovoltage, and (c) light intensity dependent V_{OC} of the control and target PSCs; UPS spectra of MeO-2PACz (d) and MeO-2PACz/3,4,5-3FPBA (e) films; energy diagrams for MeO-2PACz/perovskite (f) and MeO-2PACz/3,4,5-3FPBA/perovskite (g) interfaces.

film has a stronger resistance to erosion. In addition, the surface roughness decreased from 4.21 to 3.70 nm after modification with 3,4,5-3FPBA (Figure 2c). This indicates that the film became smoother and denser, which would facilitate the growth and crystallization of perovskite.

To further analyze the effect of 3,4,5-3FPBA modification on the growth and film formation of perovskite, SEM testing was conducted to characterize the morphology of the top and buried interfaces. Figure 2d shows that after modification with 3,4,5-3FPBA, the grain size at the top interface of the perovskite layer increased and the number of gaps at the interface reduced. These improvements will contribute to enhance the efficiency and stability of the device. Additionally, Figure 2e presents SEM images of the buried interface of the perovskite layer with and without 3,4,5-3FPBA modification. The stripping steps for the buried interface of the perovskite layer can be referenced in Figure S9. The results revealed that after modification with 3,4,5-3FPBA, the residual PbI_2 at the interface is significantly reduced. Consequently, the enhancement of the device performance can be attributed to the improved quality of perovskite thin films. The improvement in the film quality is also reflected in X-ray diffraction (XRD) measurements. As shown in Figure 3a and Table S5, the PbI_2 characteristic diffraction peaks of MeO-2PACz are observed to slightly intensify while PbI_2 signal become weaker after being deposited on MeO-2PACz and 3,4,5-3FPBA substrate, indicating that 3,4,5-3FPBA is helpful in increasing the crystallinity of the perovskite film and suppressing the formation of PbI_2 phases.

Changes in the film quality also influence exciton transport to a certain extent. Steady-state photoluminescence (PL) and time-resolved PL (TRPL) spectra were performed to characterize the transport of charge carriers. In Table S6, the rapid decay lifetime decreased from 12.50 to 10.26 ns after 3,4,5-3FPBA modification. Meanwhile, Figure 3b demonstrates the acceleration of carrier extraction and transport rates after modification with 3,4,5-3FPBA. The faster fluorescence quenching of the PL signal in (Figure 3c) verifies the results from the TRPL analysis, the red-shift of the PL peak also partly proves that nonradiative recombination is suppressed. Addi-

https://doi.org/10.1021/acsami.4c21627
ACS Appl. Mater. Interfaces 2025, 17, 16844−16854

tionally, the decrease in PL intensity after the introduction of 3,4,5-3FPBA could be due to a quenching effect caused by the presence of 3,4,5-3FPBA. Specifically, the passivation material itself may absorb some of the emitted photons or trigger other recombination processes, thereby reducing the PL intensity.

In summary, the X-ray photoelectron spectroscopy (XPS) (Figure 3d,e) analysis provides further evidence for the beneficial effects of 3,4,5-3FPBA modification on the perovskite film. The peak positions of I 3d shift from 630.72 and 619.15 to 630.21 and 618.64 eV, while the peak positions of Pb 4f shift from 137.94 and 142.92 to 137.49 and 142.42 eV. The observed shifts in Pb and I peak positions confirm the formation of coordination bonds between 3,4,5-3FPBA and perovskite.[37]

3.3. Utilization of 3,4,5-3FPBA as Dipole Chemical Bridge to Enhance the Device Efficiency. The improvement in the device performance stems partly from the enhanced quality of perovskite thin films and may also be associated with changes in the carrier dynamics of the device. To investigate whether 3,4,5-3FPBA affects the carrier dynamics processes in the devices, relevant tests are conducted. First, the EQE and integrated *J*sc values of the PSCs were measured (Figure S10). Combining Table 1 and Figure S10, the current densities of the unmodified and modified groups under $J-V$ scan tests are 23.05 and 23.47 mA/cm^2, respectively, while the EQE integrated currents are 23.25 and 23.59 mA/cm^2, respectively. The overall error between the two is less than 5%, indicating that the data are authentic and valid. Moreover, the EQE of the device after 3,4,5-3FPBA interface modification is significantly higher than that of the control device in the short wavelength range of 350−450 nm, suggesting that the recombination at the interface is suppressed. The dark $J-V$ curve in Figure 4a reveals that the device exhibits lower leakage current in the negative voltage region, indicating that 3,4,5-3FPBA modification can effectively reduce series resistance and promote hole collection and transport. The photovoltage decay of the devices was analyzed by fitting the data using a single-exponential decay model. Figure 4b shows the charge carrier recombination time constant (τ_R) extracted from the photovoltage decay measurements. After modification with 3,4,5-3FPBA, τ_R increased from 68.15 to 96.95 μs. The prolonged photovoltage decay time indicates that there is less charge recombination at the MeO-2PACz/Perovskite interface. This is mainly attributed to the effective passivation of trap defect states at the perovskite film. Transient photocurrent (TPC) measurements (Figure S11) yield similar results, and τ_R decreased from 7.62 to 3.62 μs. In addition, the interfacial charge transport and recombination were further investigated by electrochemical impedance spectroscopy. The Nyquist plots were fitted using the equivalent-circuit model shown in the inset of Figure S12, and the results were obtained (Table S7). Compared with the control device, the resistance of the device with the introduced 3,4,5-3FPBA interface modification layer significantly changed. Specifically, both the series resistance (R_s) and the transfer resistance (R_{tr}) dropped from 8.58 and 124.1 to 6.29 and 102.1 Ω, respectively. Meanwhile, the recombination resistance (R_{rec}) increased from 763 to 1222 Ω, indicating that the carrier recombination at the interface has been effectively alleviated. These results suggest that the 3,4,5-3FPBA interfacial modification layer can effectively passivate interfacial defects and accelerate carrier transport and extraction.

To verify the relationship between defect reduction in perovskite films and nonradiative recombination in devices, J_{SC} and V_{OC} measurements were performed on the devices under different light intensities. Under open-circuit conditions, V_{OC} can be described by eq 1

$$V_{OC} = \frac{nk_BT\ln\left(\frac{J_{ph}}{J_0} + 1\right)}{q} \quad (1)$$

where n is the ideal factor representing the charge carrier recombination rate, k_B is the Boltzmann constant, T is the temperature in Kelvin, J_{ph} is the photocurrent density, and J_0 is the reverse saturation current density. Figure 4c shows that after modification with 3,4,5-3FPBA, the slope of the device decreases from 1.86 to 1.53 k_BT/q. A smaller n value indicates lower trap defect recombination in the device. Meanwhile, J_{ph} (Figure S13) exhibits a linear relationship with light intensity indicating that monomolecular recombination is negligible.[38]

To get a deep insight into the influence of the interfacial dipoles on device performance, ultraviolet photoelectron spectroscopy (UPS) tests were conducted for the ITO/NiOx/MeO-2PACz films with or without a 3,4,5-3FPBA modification layer. Figure 4d,e presents the UPS results that the Fermi energy (EF) of the MeO-2PACz before modification is 4.62 eV. After introducing the interfacial layer, EF increases to 4.76 eV. This change in EF indicates a variation in the energy distribution and occupation state of electrons in the material. The energy band gap between EF and the valence band maximum (VBM) decreases from 0.85 to 0.78 eV, moving closer to the VBM. Further analysis Figure 4f,g indicates that after interfacial modification, the VBM energy level shifts from −5.47 to −5.54 eV, and the energy level offset (ΔE) decreases from 0.29 to 0.22 eV. This suggests a reduction in hole accumulation at the interface, effectively improving hole extraction and transport efficiency. It also suppresses nonradiative recombination at the interface, thereby enhancing device efficiency. In addition, the energy level change diagram (Figure S14) was plotted based on the UPS results, and the results are consistent with the above.

3.4. Improvement of Perovskite Buried Interfaces Using 3,4,5-3FPBA to Enhance Device Stability. Compared with the device efficiency, stability is more important for future development. First, device with the structure of ITO/NiOx/MeO-2PACz/$Cs_{0.05}FA_{0.82}MA_{0.13}Pb(I_{0.85}Br_{0.15})_3$/PEACL/$PC_{61}BM$/BCP/Ag was prepared to verify its performance changes under the condition of heating at 85 °C or illumination. As shown in (Figure S15), the Ag electrode device undergoes severe device decay under continuous heating at 85 °C. The device efficiency loss of 50% occurs in the first 30 min and completely fails after 30 h. Figure S16 shows that the device completely fails after 37 h of illumination and the perovskite has completely decomposed, which is obviously reflected in the SEM (Figure S17). Therefore, the presence of the Ag electrode is the primary reason for the poor stability of the device. To mitigate the negative impact of electrodes, TCO electrodes were chosen over Ag electrodes for device fabrication. The performance parameters are shown in Table S8. It can be seen that J_{SC} and FF of the TCO electrode device have decreased to different degrees compared to the Ag electrode device.

To further investigate whether 3,4,5-3FPBA interface modification can enhance the thermal stability of the device

https://doi.org/10.1021/acsami.4c21627
ACS Appl. Mater. Interfaces 2025, 17, 16844−16854

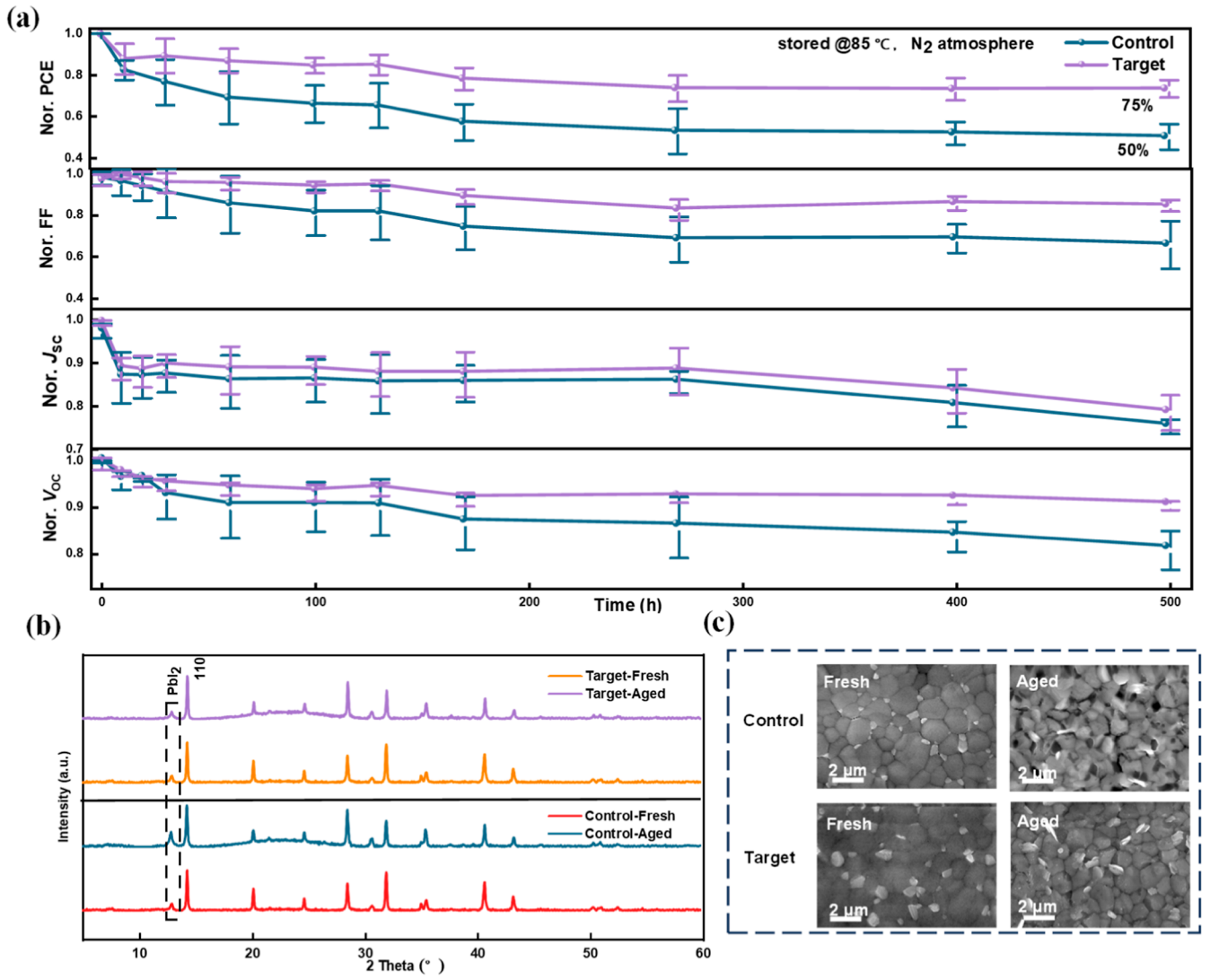

Figure 5. (a) Decay curves of PCE, FF, J_{SC}, and V_{OC} of control and target devices under continuous heating at 85 °C; and (b) XRD images and SEM images (c) of the perovskite films for the control and target devices before and after heating at 85 °C for 500 h.

at 85 °C, relevant tests were performed using the TCO electrode devices. Figure 5a shows the thermal stability decay curves of the control and target devices. It is observed that the device performance experiences a relatively rapid degradation within the first 100 h. The previous report of research group referred to this as the "burn in" phenomenon.[39] Through the analysis of various parameters, it is found that this is mainly caused by the degradation of the current. The mainly due to the ion migration inside the perovskite and at the interface in the early stage of heating. Meanwhile, as can be seen from Figure S3, this phenomenon also exists in the Ag electrode devices. However, after the 3,4,5-3FPBA interface modification, the degradation rate significantly decreases, further demonstrating that the interface modification can play a role in inhibiting the decomposition of perovskite in both the early and middle stages.

After 500 h of continuous heating, the efficiency of the target device remained at 75% of its initial efficiency, while the efficiency of the control device only maintained 50%. Additionally, the target device exhibited smaller decay degrees in V_{OC}, FF, and J_{SC} compared to the control device. This is also reflected in the initial and aged $J-V$ curves of the devices (Figure S18), indicating that 3,4,5-3FPBA can significantly improve the thermal stability of the device.

To analyze the microscopic mechanism of how 3,4,5-3FPBA enhances the stability of the device, XRD and SEM tests were performed on the aged devices. Figure 5b and Table S9 show the phase diffraction peak intensities of the perovskite films before and after aging. There are distinct peak positions at 12.8, 14.0, and 28.0° corresponding to the PbI_2 peak position and the (100) and (020) crystal planes of the perovskite cubic phase, as reported in the literature.[40] The appearance of the PbI_2 peak position may be due to excessive PbI_2 in the perovskite precursor solution, while the presence of peaks at 14.0 and 28.0° indicates that 3,4,5-3FPBA does not affect the growth and crystallization of perovskite. Further analysis of the aged XRD images revealed that the diffraction peak intensity is 408 for the control and 191 for the target at 12.8°. It suggests that the perovskite has decomposed and released PbI_2. This is more intuitively reflected in the SEM image (Figure 5c), where a large number of voids appear on the surface of the perovskite film of the unmodified device. While the perovskite grains of the modified device remain intact, the film morphology remains unchanged. These results demonstrate that the

https://doi.org/10.1021/acsami.4c21627
ACS Appl. Mater. Interfaces 2025, 17, 16844−16854

3,4,5-3FPBA interface modification layer can not only passivate relevant interface defects but also inhibit the decomposition of perovskite. In addition, ion migration is also a major factor affecting the stability of the devices. To investigate the distribution of ions within the device before and after aging, TOF-SIMS tests were performed on the above devices (Figure S19). Although the test results did not provide effective information, according to literature reports, the migration of harmful ions remains an important factor influencing device stability.

In addition, the device in an inert atmosphere tests the PCE evolution under continuous operation at the maximum power point with irradiation of a white light LED (simulating intensity of 100 mW cm^{-2}) and at an elevated temperature (55−65 °C). To facilitate the analysis of the true nature of the data, two sets of curves were plotted for the modified group and the unmodified group (both consisting of four devices), namely, the normalized curve (Figure S20) and the non-normalized curve (Figure S21). From the normalized curve, it can be observed that the modified group and the unmodified group exhibit similar attenuation trends. However, it can still be noticed that within the first 300 h, the efficiency attenuation of the modified group is lower than that of the unmodified group. This is also reflected in the initial and aged $J-V$ curves of the devices (Figure S22). After 500 h of aging, the unmodified device shows yellow PbI_2 substances near the TCO electrode (Figure S23), whereas the modified device does not exhibit this phenomenon. The precipitation of a large amount of PbI_2 can cause fatal damage to the device performance. On the one hand, it indicates that the perovskite phase has changed. On the other hand, the excess PbI_2 accumulating at the interface will form defect recombination centers, thereby leading to a decline in device stability. Meanwhile, upon observing the non-normalized stability attenuation curves, it is found that compared with the modified group, the unmodified group shows larger errors in V_{OC}, J_{SC}, and FF. This is not conducive to the equalization of devices. The large errors indicate that there is no uniform attenuation among different devices, which is detrimental to the commercial application and large-scale development of devices. The abovementioned analysis proves the importance of the 3,4,5-3FPBA interface modification. It also shows that this modification can inhibit the decomposition of perovskite and the precipitation of PbI_2 under illumination.

4. CONCLUSIONS

In summary, this work successfully introduced small molecule 3,4,5-3FPBA into PSCs as an interfacial modification layer between the SAM layer and the perovskite layer. Through 3,4,5-3FPBA interface modification, the perovskite grain size increases, the grain boundaries decrease, and the buried defects are reduced, resulting in faster overall carrier transport and charge extraction. There are fewer interface defects between the perovskite layer and the underlying interface. The results demonstrate that the 3,4,5-3FPBA-modified device achieves best efficiency of 24.02% based on the perovskite composition $Cs_{0.05}(FA_{0.98}MA_{0.02})_{0.95}Pb(I_{0.95}Br_{0.05})_3$. The unencapsulated device can still maintain 75% of its initial efficiency after continuous heating at 85 °C for 500 h for the perovskite composition $Cs_{0.05}FA_{0.82}MA_{0.13}Pb(I_{0.85}Br_{0.15})_3$. This interfacial modification strategy provides a simple and convenient method to address the thermal stability issue in inverted PSCs.

ASSOCIATED CONTENT

Supporting Information

The Supporting Information is available free of charge at https://pubs.acs.org/doi/10.1021/acsami.4c21627.

SEM cross-sectional images of standard devices and perovskite films with Ag electrodes after aging; performance parameter statistics of devices after modification with different fluorobenzeneboronic acid small molecules; corresponding hysteresis coefficient and short-term thermal stability change curves; hysteresis coefficient and corresponding performance parameters of 3,4,5-3FPBA-modified and original devices at different scan rates; EQE, TPC, impedance, relationship between J_{SC} and light intensity, short-term 85 °C thermal stability curve, light stability curve, long-term 85 °C thermal stability curve, and light stability curve for 3,4,5-3FPBA-modified and original devices; $J-V$ curves for 1 cm^2 devices; UV absorption and transmission for 3,4,5-3FPBA-modified and original perovskite films; TOF-SIMS characterization of ion distribution before and after device heating aging; $J-V$ curves before and after device heating and light aging; device photographs after light aging; energy level diagram after introducing 3,4,5-3FPBA; perovskite buried bottom cross-section peeling method; thickness of each transport layer; performance parameters, TRPL fitting parameters, and impedance spectrum fitting parameters for 3,4,5-3FPBA-modified and original devices; and phase diffraction peak intensity for 3,4,5-3FPBA-modified and original perovskite films (PDF)

AUTHOR INFORMATION

Corresponding Authors

Changzeng Ding − *i-Lab & Printable Electronics Research Center, Suzhou Institute of Nano-Tech and Nano-Bionics, Chinese Academy of Sciences, Suzhou 215123, P. R. China; Physics and Center for Functional Materials Faculty of Science and Technology Åbo Akademi University, Turku 20500, Finland*; Email: czding2017@sinano.ac.cn

Yongzhen Yang − *Key Laboratory of Interface Science and Engineering in Advanced Materials, Ministry of Education, Taiyuan University of Technology, Taiyuan, Shanxi 030024, China; Shanxi-Zheda Institute of Advanced Materials and Chemical Engineering, Taiyuan 030032, P. R. China;* orcid.org/0000-0003-0566-4802; Email: yangyongzhen@tyut.edu.cn

Chang-Qi Ma − *i-Lab & Printable Electronics Research Center, Suzhou Institute of Nano-Tech and Nano-Bionics, Chinese Academy of Sciences, Suzhou 215123, P. R. China;* orcid.org/0000-0002-9293-5027; Email: cqma2011@sinano.ac.cn

Authors

Jiansheng Yang − *Key Laboratory of Interface Science and Engineering in Advanced Materials, Ministry of Education, Taiyuan University of Technology, Taiyuan, Shanxi 030024, China; i-Lab & Printable Electronics Research Center, Suzhou Institute of Nano-Tech and Nano-Bionics, Chinese Academy of Sciences, Suzhou 215123, P. R. China*

Zhenhua Zhao − *i-Lab & Printable Electronics Research Center, Suzhou Institute of Nano-Tech and Nano-Bionics, Chinese Academy of Sciences, Suzhou 215123, P. R. China*

https://doi.org/10.1021/acsami.4c21627
ACS Appl. Mater. Interfaces 2025, 17, 16844−16854

Lianping Zhang − *i-Lab & Printable Electronics Research Center, Suzhou Institute of Nano-Tech and Nano-Bionics, Chinese Academy of Sciences, Suzhou 215123, P. R. China*
Xiaomei Gao − *i-Lab & Printable Electronics Research Center, Suzhou Institute of Nano-Tech and Nano-Bionics, Chinese Academy of Sciences, Suzhou 215123, P. R. China*
Rong Huang − *Vacuum Interconnected Nanotech Workstation (Nano-X), Suzhou Institute of Nano-Tec and Nano-Bionics, Chinese Academy of Sciences, Suzhou 215123, P. R. China*
Zhiyun Li − *Vacuum Interconnected Nanotech Workstation (Nano-X), Suzhou Institute of Nano-Tec and Nano-Bionics, Chinese Academy of Sciences, Suzhou 215123, P. R. China*
Qun Luo − *i-Lab & Printable Electronics Research Center, Suzhou Institute of Nano-Tech and Nano-Bionics, Chinese Academy of Sciences, Suzhou 215123, P. R. China;* orcid.org/0000-0002-7527-460X
Bin Fan − *Kunshan GCL Optoelectronic Materials Co., Ltd, Kunshan, Jiangsu 215300, P. R. China*
Qingyong Tian − *Kunshan GCL Optoelectronic Materials Co., Ltd, Kunshan, Jiangsu 215300, P. R. China*
Lingpeng Yan − *Key Laboratory of Interface Science and Engineering in Advanced Materials, Ministry of Education, Taiyuan University of Technology, Taiyuan, Shanxi 030024, China; College of Materials Science and Engineering, Taiyuan University of Technology, Taiyuan 030024, P. R. China;* orcid.org/0000-0003-1177-8558
Kunpeng Guo − *Key Laboratory of Interface Science and Engineering in Advanced Materials, Ministry of Education, Taiyuan University of Technology, Taiyuan, Shanxi 030024, China;* orcid.org/0000-0003-2075-6000

Complete contact information is available at: https://pubs.acs.org/10.1021/acsami.4c21627

Author Contributions

J.Y., Z.Z., and C.D. contributed to data management, formal analysis, investigation, methodology, and manuscript writing. X.G. contributed to software and visualization. L.Z., R.H., and Z.L. contributed to data management and formal analysis. B.F. and Q.T. contributed to data management. C.D., C.M., Q.L., L.Y., and K.G. contributed to formal analysis, investigation, methodology, writing—review and editing, conceptualization, and funding acquisition. Y.Y., C.D., and C.M. contributed to resources, supervision, validation, and writing—review and editing.

Notes

The authors declare no competing financial interest.

ACKNOWLEDGMENTS

The authors would like to acknowledge the financial support from the National Natural Science Foundation of China (22109172, 22135001, and 22372114), the Jiangsu Science and Technology Program (BE2022021), the China Postdoctoral Science Foundation (2023T160469 and 2023M732554), and the Shanxi-Zheda Institute of Advanced Materials and Chemical Engineering (2022SX-TD012 and 2021SX-TD012). The authors are grateful for the technical support from the Suzhou Institute of Nano-Tech and Nano-Bionics for the TOF-SIMS and XPS testing in Nano-X.

REFERENCES

(1) Luo, X. H.; Liu, X.; Lin, X. S.; Wu, T. H.; Wang, Y. B.; Han, Q. F.; Wu, Y. Z.; Segawa, H.; Han, L. Y. Recent Advances of Inverted Perovskite Solar Cells. *ACS Energy Lett.* **2024**, *9* (4), 1487−1506.
(2) Li, Y.; Wang, Y. H.; Xu, Z. C.; Peng, B.; Li, X. F. Key Roles of Interfaces in Inverted Metal-Halide Perovskite Solar Cells. *ACS Nano* **2024**, *18* (16), 10688−10725.
(3) Suo, J. J.; Yang, B. W.; Bogachuk, D.; Boschloo, G.; Hagfeldt, A. The Dual Use of SAM Molecules for Efficient and Stable Perovskite Solar Cells. *Adv. Energy Mater.* **2024**, *15*, 2400205.
(4) Miah, M. H.; Khandaker, M. U.; Rahman, M. B.; Nur-E-Alam, M.; Islam, M. A. Band gap tuning of perovskite solar cells for enhancing the efficiency and stability: issues and prospects. *RSC Adv.* **2024**, *14* (23), 15876−15906.
(5) Xu, Z. Y.; Zhuang, Q. X.; Zhou, Y. Q.; Lu, S. R.; Wang, X. H.; Cai, W. S.; Zang, Z. G. Functional Layers of Inverted Flexible Perovskite Solar Cells and Effective Technologies for Device Commercialization. *Small Struct.* **2023**, *4* (5), 2200338.
(6) Jiang, Y.; Qi, Y. B. Metal halide perovskite-based flexible tandem solar cells: next-generation flexible photovoltaic technology. *Mater. Chem. Front.* **2021**, *5* (13), 4833−4850.
(7) Chen, H.; Liu, C.; Xu, J.; Maxwell, A.; Zhou, W.; Yang, Y.; Zhou, Q. L.; Bati, A. S. R.; Wan, H. Y.; Wang, Z. W.; Zeng, L. W.; Wang, J. K.; Serles, P.; Liu, Y.; Teale, S.; Liu, Y. J.; Saidaminov, M. I.; Li, M. Z.; Rolston, N.; Hoogland, S.; Filleter, T.; Kanatzidis, M. G.; Chen, B.; Ning, Z. J.; Sargent, E. H. Improved charge extraction in inverted perovskite solar cells with dual-site-binding ligands. *Science* **2024**, *384* (6692), 189−193.
(8) Wang, J.; Zhu, J.; Chen, C.; Paetzold, U. W.; Zhao, D. Development and Challenges of Large-Area All-Perovskite Tandem Solar Cells and Modules. *Sol. RRL* **2024**, *8* (21), 2301066.
(9) Liu, C.; Yang, T.; Cai, W.; Wang, Y.; Chen, X.; Wang, S.; Huang, W.; Du, Y.; Wu, N.; Wang, Z.; Yang, Y.; Feng, J.; Niu, T.; Ding, Z.; Zhao, K. Flexible Indoor Perovskite Solar Cells by In Situ Bottom-Up Crystallization Modulation and Interfacial Passivation. *Adv. Mater.* **2024**, *36* (24), 2311562.
(10) Ren, H.; Chen, W. S.; Chen, J. D.; Yang, J. P.; Zhang, Y. F.; Hou, H. Y.; Tian, S.; Ge, H. R.; Li, Y. Q.; Tang, J. X. Unraveling the electrical energy loss in silver nanowire electrodes for flexible and Large-Area organic solar cells. *Chem. Eng. J.* **2024**, *481*, 148498.
(11) Wang, Y.; Zhou, S.; Liu, X.; Sun, K.; Lee, M.; Liu, Z.; Zhang, M.; Bai, Y.; Hameiri, Z.; Hao, X. Cu_2(Thiourea)Br_2 Complex as a Multifunctional Interfacial Layer for Reproducible PTAA-Based p−i−n Perovskite Solar Cells. *Cells* **2024**, *8* (5), 2300920.
(12) Jiang, J.; Wang, X. Z.; Li, A. J.; Song, J. X.; Wang, X. F. Enhanced Photovoltaic Performance by Improved Hole Extraction with a Molecule Dopant in Inverted Perovskite Solar Cells. *ACS Appl. Energy Mater.* **2024**, *7* (9), 3996−4003.
(13) Wei, J. Y.; Chen, L. J.; Lei, Y. L.; Tan, X. W.; Zhang, Q. M. Improving the Performance of Perovskite Solar Cells with Sodium Stearate-Doped PEDOT:PSS as a Hole Transport Layer. *ACS Appl. Polym. Mater.* **2024**, *6* (4), 2085−2092.
(14) Li, X. M.; Tang, Y.; Song, B.; Meng, F. W.; Gao, C.; Qin, L.; Hu, Y. F.; Lou, Z. D.; Teng, F.; Hou, Y. B. Efficient Tin-Based Perovskite Solar Cell with a Cesium Acetate Pre-buried PEDOT:PSS Hole Transport Layer. *J. Phys. Chem. Lett.* **2024**, *15* (5), 1355−1362.
(15) Zhou, Y.; Huang, X.; Zhang, J.; Zhang, L.; Wu, H.; Zhou, Y.; Wang, Y.; Wang, Y.; Fu, W.; Chen, H. Interfacial Modification of NiOx for Highly Efficient and Stable Inverted Perovskite Solar Cells. *Adv. Energy Mater.* **2024**, *14* (25), 2400616.
(16) Yan, N.; Cao, Y.; Jin, Z.; Liu, Y.; Liu, S.; Fang, Z.; Feng, J. Surface Reconstruction for Efficient NiO_x-Based Inverted Perovskite Solar Cells. *Adv. Mater.* **2024**, *36* (31), 2403682.
(17) Cao, Q.; Wang, T.; Pu, X.; He, X.; Xiao, M.; Chen, H.; Zhuang, L.; Wei, Q.; Loi, H.-L.; Guo, P.; Kang, B.; Feng, G.; Zhuang, J.; Feng, G.; Li, X.; Yan, F. Co-Self-Assembled Monolayers Modified NiO_x for Stable Inverted Perovskite Solar Cells. *Adv. Mater.* **2024**, *36* (16), 2311970.

(18) Chen, M.; Kapil, G.; Wang, L.; Razey Sahamir, S.; Baranwal, A. K.; Nishimura, K.; Sanehira, Y.; Zhang, Z.; Akmal Kamarudin, M.; Shen, Q.; Hayase, S. High performance wide bandgap Lead-free perovskite solar cells by monolayer engineering. *Chem. Eng. J.* **2022**, *436*, 135196.
(19) Zhao, J. T.; Yang, X.; Zhou, W. B.; Wang, R. B.; Wang, Y.; Zhang, J. W.; Zhong, X. Y.; Ren, H. Z.; Hou, G. F.; Ding, Y.; Zhao, Y.; Zhang, X. D. Performance Amelioration of Spray-Coated Perovskite Solar Cells Utilizing a Self-Assembled Monolayer. *ACS Appl. Energy Mater.* **2024**, *7* (9), 3540−3549.
(20) Ou, Y. L.; Huang, H.; Shi, H. X.; Li, Z. Y.; Chen, Z. J.; Mateen, M.; Lu, Z. B.; Chi, D.; Huang, S. H. Collaborative interfacial modification and surficial passivation for high-efficiency MA-free wide-bandgap perovskite solar cells. *Chem. Eng. J.* **2023**, *469*, 143860.
(21) Almasabi, K.; Zheng, X. P.; Turedi, B.; Alsalloum, A. Y.; Lintangpradipto, M. N.; Yin, J.; Gutierrez-Arzaluz, L.; Kotsovos, K.; Jamal, A.; Gereige, I.; Mohammed, O. F.; Bakr, O. M. Hole-Transporting Self-Assembled Monolayer Enables Efficient Single-Crystal Perovskite Solar Cells with Enhanced Stability. *ACS Energy Lett.* **2023**, *8* (2), 950−956.
(22) Kim, D.-H.; Lee, H.-J.; Lee, S.-H.; Kang, Y.-J.; Kwon, S.-N.; Kim, D.-H.; Na, S.-I. Mixed Self-Assembled Hole-Transport Monolayer Enables Simultaneous Improvement of Efficiency and Stability of Perovskite Solar Cells. *Cells* **2024**, *8* (9), 2400067.
(23) Hossain, K.; Kulkarni, A.; Bothra, U.; Klingebiel, B.; Kirchartz, T.; Saliba, M.; Kabra, D. Resolving the Hydrophobicity of the Me-4PACz Hole Transport Layer for Inverted Perovskite Solar Cells with Efficiency > 20%. *ACS Energy Lett.* **2023**, *8* (9), 3860−3867.
(24) Kulkarni, A.; Sarkar, R.; Akel, S.; Häser, M.; Klingebiel, B.; Wuttig, M.; Wiegand, S.; Chakraborty, S.; Saliba, M.; Kirchartz, T. A Universal Strategy of Perovskite Ink- Substrate Interaction to Overcome the Poor Wettability of a Self-Assembled Monolayer for Reproducible Perovskite Solar Cells. *Cells* **2023**, *33* (47), 2305812.
(25) Lee, S.-H.; Lee, H.-J.; Kim, D.-H.; Noh, Y.-J.; Kwon, S.-N.; Kim, D.-H.; Na, S.-I. Vacuum-Assisted Deposition of Highly Hydrophobic Self-Assembled Monolayer for High-Efficiency Perovskite Solar Cells. *Cells* **2024**, *8* (11), 2400170.
(26) Li, C.; Zhang, K.; Maiti, S.; Peng, Z.; Tian, J.; Park, H.; Byun, J.; Xie, Z.; Dong, L.; Qiu, S.; Bornschlegl, A. J.; Liu, C.; Zhang, J.; Osvet, A.; Heumueller, T.; Christiansen, S. H.; Halik, M.; Unruh, T.; Li, N.; Lüer, L.; Brabec, C. J. Tailoring the Dimensionality of 2D/3D Heterojunctions for Inverted Perovskite Solar Cells. *ACS Energy Lett.* **2024**, *9* (3), 779−788.
(27) Li, H. S.; Liu, S. C. Revolutionary SAMs: transforming inverted perovskite solar cells. *J. Mater. Chem. A* **2024**, *12* (17), 9929−9932.
(28) Zeng, L.; Tang, L. T.; Luo, Z. K.; Gong, J. B.; Li, J. M.; Xiao, X. D. A Review of Perovskite/Copper Indium Gallium Selenide Tandem Solar Cells. *Sol. RRL* **2024**, *8* (21), 2301059.
(29) Li, Z.; Sun, X. L.; Zheng, X. P.; Li, B.; Gao, D. P.; Zhang, S. F.; Wu, X.; Li, S.; Gong, J. Q.; Luther, J. M.; Li, Z. A.; Zhu, Z. L. Stabilized hole-selective layer for high-performance inverted p-i-n perovskite solar cells. *Science* **2023**, *382* (6668), 284−289.
(30) Mohamad Noh, M. F.; Arzaee, N. A.; Harif, M. N.; Mat Teridi, M. A.; Mohd Yusoff, A. R. b.; Mahmood Zuhdi, A. W. Defect Engineering at Buried Interface of Perovskite Solar Cells. *Small Methods* **2024**, *8* (12), 2400385.
(31) Ruan, C.; He, L.; Zhu, L.; Yuan, B.; Yang, H.; Qin, G.; Chen, Y.; Tao, Q. Advancements and future directions in defect passivation for perovskite solar cells. *J. Alloys Compd.* **2024**, *999*, 174990.
(32) Tang, H. C.; Shen, Z. C.; Shen, Y. Z.; Yan, G.; Wang, Y. B.; Han, Q. F.; Han, L. Y. Reinforcing self-assembly of hole transport molecules for stable inverted perovskite solar cells. *Science* **2024**, *383* (6688), 1236−1240.
(33) Zhang, W. X.; Guo, X. M.; Cui, Z. B.; Yuan, H. B.; Li, Y. F.; Li, W.; Li, X. D.; Fang, J. F. Strategies for Improving Efficiency and Stability of Inverted Perovskite Solar Cells. *Adv. Mater.* **2024**, *36* (37), 2311025.
(34) Zhu, S. J.; Wu, J. H.; Sun, W. H.; Pan, W. C.; Cai, F. F.; Liu, J. M.; Chen, L. Q.; Chen, X.; Wang, C. Y.; Wang, X. B. Interlayer Modification Using Phenylethylamine Tetrafluoroborate for Highly Effective Perovskite Solar Cells. *ACS Appl. Energy Mater.* **2022**, *5* (1), 658−666.
(35) Zhang, Y.; Yu, R.; Li, M.; He, Z.; Dong, Y.; Xu, Z.; Wang, R.; Ma, Z.; Tan, Z. Amphoteric Ion Bridged Buried Interface for Efficient and Stable Inverted Perovskite Solar Cells. *Adv. Mater.* **2023**, *36* (1), 2310203.
(36) Qiu, J.; Mei, X.; Zhang, M.; Wang, G.; Zou, S.; Wen, L.; Huang, J.; Hua, Y.; Zhang, X. Dipolar Chemical Bridge Induced CsPbI3 Perovskite Solar Cells with 21.86% Efficiency. *Angew. Chem., Int. Ed.* **2024**, *63* (18), No. e202401751.
(37) Yin, R.; Wu, R. F.; Miao, W. J.; Wang, K. X.; Sun, W. W.; Huo, X. A.; Sun, Y. S.; You, T. T.; Hao, W. C.; Yin, P. G. Enhanced anchoring enables highly efficient and stable inverted perovskite solar cells. *Nano Energy* **2024**, *125*, 109544.
(38) Johnston, M. B.; Herz, L. M. Hybrid Perovskites for Photovoltaics: Charge-Carrier Recombination, Diffusion, and Radiative Efficiencies. *Acc. Chem. Res.* **2016**, *49* (1), 146−154.
(39) Ding, C.; Yin, L.; Wang, J.; Larini, V.; Zhang, L.; Huang, R.; Nyman, M.; Zhao, L.; Zhao, C.; Li, W.; Luo, Q.; Shen, Y.; Österbacka, R.; Grancini, G.; Ma, C.-Q. Boosting Perovskite Solar Cells Efficiency and Stability: Interfacial Passivation of Crosslinked Fullerene Eliminates the Burn-in Decay. *Adv. Mater.* **2023**, *35* (2), 2207656.
(40) Li, X.; Ding, C.; Yin, L.; Zhang, L.; Yang, Y.; Yan, L.; Ma, C.-Q. Stabilizing formamidinium lead triiodide α-phase with diamine cations for perovskite solar cells. *Chem. Eng. J.* **2023**, *472*, 145024.

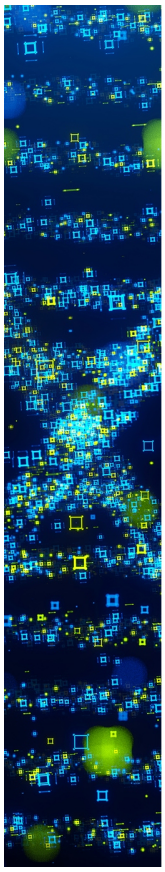

https://doi.org/10.1021/acsami.4c21627
ACS Appl. Mater. Interfaces 2025, 17, 16844−16854